ROYAL SOCIETY OF CHEMISTRY

## PAPER

Check for updates

# Tunable physical properties in Bi-based layered supercell multiferroics embedded with Au nanoparticles†

Jianan Shen, [ID] [a] Zihao He,[b] Di Zhang, [ID] [a] Ping Lu,[c] Julia Deitz,[c] Zhongxia Shang,[a] Matias Kalaswad,[b] Haohan Wang,[d] Xiaoshan Xu [ID] [d] and Haiyan Wang [ID] ⋆[ab]

Multiferroic materials are an interesting functional material family combining two ferroic orderings, *e.g.*, ferroelectric and ferromagnetic orderings, or ferroelectric and antiferromagnetic orderings, and find various device applications, such as spintronics, multiferroic tunnel junctions, *etc.* Coupling multiferroic materials with plasmonic nanostructures offers great potential for optical-based switching in these devices. Here, we report a novel nanocomposite system consisting of layered $Bi_{1.25}AlMnO_{3.25}$ (BAMO) as a multiferroic matrix and well dispersed plasmonic Au nanoparticles (NPs) and demonstrate that the Au nanoparticle morphology and the nanocomposite properties can be effectively tuned. Specifically, the Au particle size can be tuned from 6.82 nm to 31.59 nm and the 6.82 nm one presents the optimum ferroelectric and ferromagnetic properties and plasmonic properties. Besides the room temperature multiferroic properties, the BAMO–Au nanocomposite system presents other unique functionalities including localized surface plasmon resonance (LSPR), hyperbolicity in the visible region, and magneto-optical coupling, which can all be effectively tailored through morphology tuning. This study demonstrates the feasibility of coupling single phase multiferroic oxides with plasmonic metals for complex nanocomposite designs towards optically switchable spintronics and other memory devices.

## Introduction

Multiferroics, with the coexistence of at least two ferroic orderings, are both scientifically and technologically important owing to the rich underlying physics and promising applications.[1–4] Since the phenomenon of multiferroics was first demonstrated in $Ni_3B_7O_{13}I$, the search for single-phase multiferroic compounds has expanded significantly.[5] $BiFeO_3$ is one of the most studied examples of single-phase multiferroic materials, yet has limitations for practical applications due to its antiferromagnetic ordering and low magnetization value.[6,7]

*aSchool of Materials Engineering, Purdue University, West Lafayette, Indiana 47907, USA. E-mail: hwang00@purdue.edu*

*bSchool of Electrical and Computer Engineering, Purdue University, West Lafayette, Indiana 47907, USA*

*cSandia National Laboratories, Albuquerque, New Mexico 87185, USA*

*dDepartment of Physics and Astronomy, University of Nebraska-Lincoln, Lincoln, Nebraska 68588, USA*

† Electronic supplementary information (ESI) available: Supplementary XRD results on the LAO substrate and other deposition temperatures; plan-view STEM images for particle size analysis; transmittance measurements on the LAO substrate and bandgap calculations using the Tauc method; 3D models of COMSOL simulation and the plasmonic response at different wavelengths; experimental ellipsometric data and fitted permittivity for BAMO-Au and pure BAMO films; saturation magnetization and coercive field measurements; curve of piezoelectric coefficient $d_{33}$ as a function of tip bias and the polarization hysteresis loop. See https://doi.org/10.1039/d2na00169a

Despite the tremendous work on searching for multiferroic material candidates, the family of single-phase multiferroic materials remains very limited.[3,4,8–10] As a new class of single phase multiferroic oxides proposed in 2010 and discovered in 2013, Bi-based layered supercell (LSC) oxides have raised enormous interest owing to their structure anisotropy and fascinating physical properties including multiferroic properties and anisotropic dielectric permittivity.[11–16] More specifically, Bi-based LSC oxides are Bi-based transition metal oxides with an Aurivillius phase.[11,13–15] Their room-temperature multiferroic properties reside in the $6s^2$ lone pair of electrons of Bi for ferroelectricity and transition magnetic ions for magnetic ordering.[11–15,17–19] For example, $Bi_2FeMnO_6$ with a 2D layered oxide structure has been demonstrated to have room-temperature ferrimagnetism and ferroelectricity.[11,17,19] Recently, a bismuth-based oxide $Bi_2AlMnO_6$ (BAMO) with an LSC structure was reported to be a multiferroic at room temperature.[13,15] These discoveries have led to new candidates and paved new design routes for room-temperature single phase multiferroic materials.

Optical based switching has been considered as one of the most superior switching mechanisms for electronic/spintronic devices due to their ultrafast switching speed and unparalleled low heating dissipation.[20] Various approaches have been used recently. For example, Lalieu *et al.* demonstrated single pulse all-optical switching along with spin Hall effect driven

magnetic domain motion in the Pt/Co/Gd stacking.[21] Aviles-Felix et al. investigated the single-shot switching of the magnetization of perpendicular magnetic tunneling junctions consisting of a Tb/Co nanolayer stacking, where the toggling of the magnetic state can be controlled by 60 fs-long or 5 ps-long laser pulses.[22] Taking advantage of the state-of-the-art thin film growth techniques, very dissimilar materials with various functionalities can be integrated on selected substrates as multifunctional nanocomposites, e.g., systems with ferromagnetic and ferroelectric coupling, and systems with magneto-optical coupling.[12,15,23–26] In general, three types of nanocomposite morphologies have been successfully fabricated using pulsed laser deposition (PLD), i.e., particle-in-matrix (PIM) structure, multilayer structure, and vertically aligned nanocomposite (VAN) structure.[23,24,27–30] Among these structures, PIM is of special interest since it allows the combination of metal NPs with the oxide matrix, forming novel thin films. For instance, Au NPs are conventional plasmonic metamaterial building blocks displaying strong localized surface plasmon resonance (LSPR) which offers a pathway to exotic optical properties and technologically important applications, such as surface-enhanced Raman scattering (SERS), optical trapping and manipulation, biosensing and nanomedicine, and magneto-plasmonic effects.[31–40] For example, the Au–$TiO_2$ system has shown enhanced photocatalytic properties and the enhancement varies as a function of Au particle size.[41] Au and Pt nanoparticles have been introduced into $VO_2$ as an effective secondary phase to reduce the phase transition temperature from 360.74 K to 329.16 K or lower.[42,43] Interesting optical dielectric function tuning has been demonstrated in multiple systems including BTO-Au, ZnO–Au, $La_{0.7}Sr_{0.3}MnO_3$–Au, etc.[44,45]

In this work, we have combined the newly discovered single phase multiferroic BAMO LSC as the matrix and the plasmonic Au NPs to form a new nanocomposite system. By coupling the room-temperature multiferroic properties of the BAMO LSC and the LSPR of Au NPs, as shown in the schematic in Fig. 1a, we are expecting enhanced anisotropic dielectric permittivity, plasmonic properties, and ferroelectric and ferromagnetic properties combined in one nanocomposite platform. By selecting different deposition temperatures (580 °C, 600 °C, and 620 °C), we hypothesize that the microstructures of the nanocomposites will be changed and thus their physical properties will be effectively tuned. Besides, the optimum deposition temperature is investigated and the physical origins of the various properties are discussed. The property tuning indicates that it's viable to tailor the physical properties through morphology evolution by controlling the deposition temperature. The study may pave a new avenue towards the design of novel thin films with multiferroic properties along with fascinating optical-based switching potential.

# Experimental section

## Composite film growth

The BAMO target used for thin film growth was fabricated by mixing $Bi_2O_3$, $Al_2O_3$, and $Mn_2O_3$ powders followed by sintering at 750 °C for 6 hours. The Au strip was attached onto the target

for deposition. The BAMO-Au thin films were deposited on single-crystal $SrTiO_3(001)$ and $LaAlO_3(001)$ substrates by pulsed laser deposition (PLD) (with a KrF excimer laser, Lambda Physik COMPex Pro 205, $\lambda = 248$ nm). The deposition temperature was controlled at 580 °C, 600 °C, and 620 °C, respectively. The background oxygen pressure was maintained at 200 mTorr. The deposition used a laser fluence of 3.6 J $cm^{-2}$ and a laser frequency of 2 Hz. Following deposition, the films were in situ annealed at 400 °C for 1 hour in 500 Torr of oxygen. Finally, the films were cooled down to room temperature at 10 °C $min^{-1}$.

## Microstructure characterization

The microstructure and crystallinity of the thin films were characterized by XRD (PANalytical Empyrean) and high-resolution STEM (Thermo Fisher Scientific TALOS 200× operated at 200 kV). An FEI Titan™ G2 80-200 STEM with a $C_s$ probe corrector and ChemiSTEM™ technology (X-FEG™ and SuperX™ energy-dispersive X-ray spectroscopy (EDS) with four windowless silicon drift detectors), operated at 200 kV, was also used in this study. The sample preparation work for STEM characterization was conducted by manual grinding and thinning procedures accompanied by dimpling and ion milling processes using a precision ion polishing instrument (PIPS II Model 695, Gatan). The energy-dispersive X-ray spectroscopy (EDS) mode in STEM was utilized to investigate the chemical composition of the thin films.

## Property measurements

Transmittance measurements were carried out using a UV-vis-NIR absorption spectrophotometer (PerkinElmer Lambda 1050). The plasmonic response was simulated using COMSOL Multiphysics® software. The dielectric permittivity was investigated by spectroscopic ellipsometry (JA Woollam RC2). The ellipsometer parameters $\Psi$ and $\Delta$, related by $r_p/r_s = \tan(\Psi)e^{i\Delta}$ (where $r_p$ and $r_s$ are reflection coefficients for the p-polarized and s-polarized light, respectively), were fitted with CompleteEASE software. The incident angle was set to 55°, 65°, and 75° for improving the accuracy of the model. The dielectric permittivity was assumed to be anisotropic owing to the layered structure of the matrix. The permittivity along the in-plane (IP) direction was modeled using one Drude oscillator and two Cody-Lorentz oscillators, and the permittivity along the out-of-plane (OP) direction was modeled using one Drude oscillator and one Cody-Lorentz oscillator. The fitted results have a mean squared error (MSE) of around 5. The magnetic properties were investigated using a vibrating sample magnetometer (VSM) in a Magnetic Property Measurement System (MPMS3, Quantum Design). The IP and OP magnetization were measured after calibrating the VSM set up for potential calibration errors including high-field slope and magnet resonance correction, and sample geometry factor calibration. In addition, multiple steps have been conducted following the acquisition of the raw data to eliminate the potential errors introduced during the measurement of the M–H curve. For example, magnetic remanence correction was implemented using a built-in
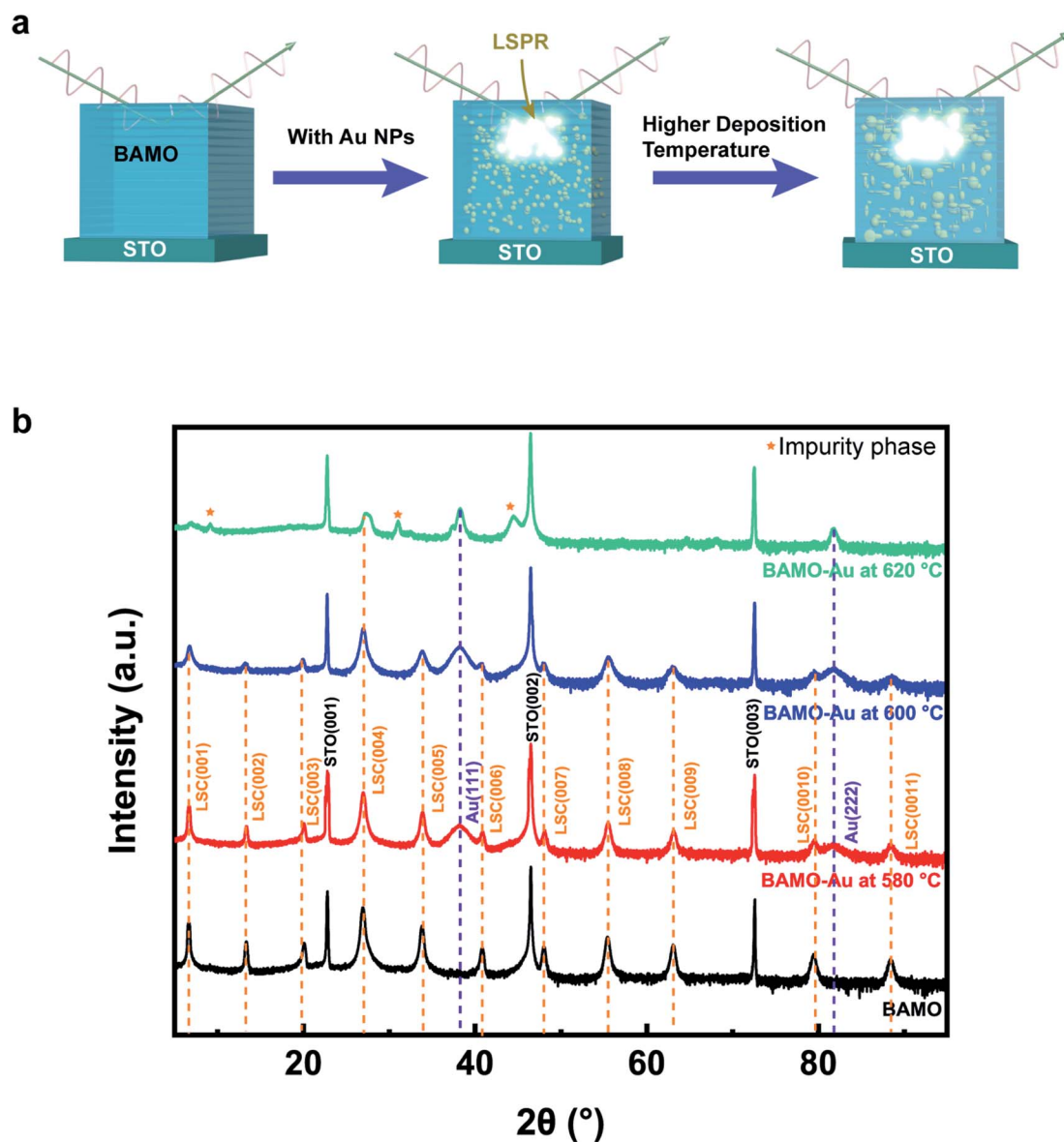
Fig. 1 (a) Schematic illustration of BAMO-Au thin films and the plasmonic behavior induced by Au NPs. (b) XRD $\theta-2\theta$ diffraction results of BAMO and BAMO-Au epitaxial thin films on the STO(001) substrate at various deposition temperatures.

script; the sample geometry multiplicative factor was obtained and applied to the measurement results using a sample geometry calculator, and the multiplicative factors for the samples vary between 0.9 and 1.2. The ferroelectric properties were examined using a Si tip coated with a conductive Pt–Ir layer (SCM-PIT V2) with a Bruker Dimension Icon AFM. A home-built MOKE system was applied with a He–Ne laser of 632.8 nm at room temperature in a polar configuration. The incident light was polarized using a linear polarizer; the Kerr rotation of the light was measured using a second polarizer assisted by a photoelastic modulator. In the polar configuration, the reflected light was separated from the normal incident light (0° incident angle) by a 50% beam splitter and the magnetic field was perpendicular to the film surface.

## Results and discussion

The epitaxial growth of the thin films was first demonstrated by XRD. Fig. 1b shows the XRD $\theta-2\theta$ scans of BAMO-Au thin films deposited on STO(001) at different temperatures, with a pure BAMO thin film as the reference. There are obvious LSC peaks as labeled in Fig. 1b suggesting highly textured growth of the layered oxides. The diffraction peaks of Au (111) and (222) were shown in the samples at all three deposition temperatures confirming the effective Au incorporation in the system. Among the various temperature conditions, the film grown at 580 °C exhibits the best growth quality which is proved by the XRD results along with HAADF-STEM results, to be discussed later. The (00l) set of peaks indicating the LSC structure of the matrix are well preserved at 580 °C. At 600 °C, the LSC structure is still

maintained but peaks become broader and the peak intensity reduces, suggesting the slightly degraded epitaxial quality of the film. Finally, most of the LSC peaks disappeared at 620 °C, manifesting the destruction of the LSC structure at this growth temperature. It is noted that there are some impurity phases at 620 °C, which could possibly be attributed to the alumina phase, aluminum manganese phase and/or aluminum bismite phase. The similar dominant (00l) diffraction peaks as shown in Fig. S1† suggest that BAMO-Au thin films were also be able to grow on the LaAlO₃ (LAO) (001) substrate with comparable film quality to those on STO substrates.

The microstructure of BAMO-Au thin films was further investigated by high-resolution STEM under the HAADF mode along with EDS mapping analysis as shown in Fig. 2 and 3.

Fig. 2b displays the cross-sectional STEM image of the BAMO-Au thin film grown on the STO(001) substrate at the deposition temperature of 580 °C. The layered supercell structure was well preserved and Au NPs were uniformly distributed in the LSC matrix. The inset is the selected area diffraction pattern (SAED) which indicates the highly epitaxial growth of the thin film. The SAED pattern and XRD results together confirm the (111)-oriented growth of Au NPs on the STO substrate. Fig. 2c–e are high-resolution STEM images and EDS maps of BAMO-Au thin films on the LAO(001) substrate. The microstructure is nearly identical to that on the STO substrate with a slight difference in the orientation of Au NPs. As shown in Fig. S1,† Au NPs have two orientations of (111) and (001) on the LAO substrate where the (111) peak is stronger than the (001) peak,
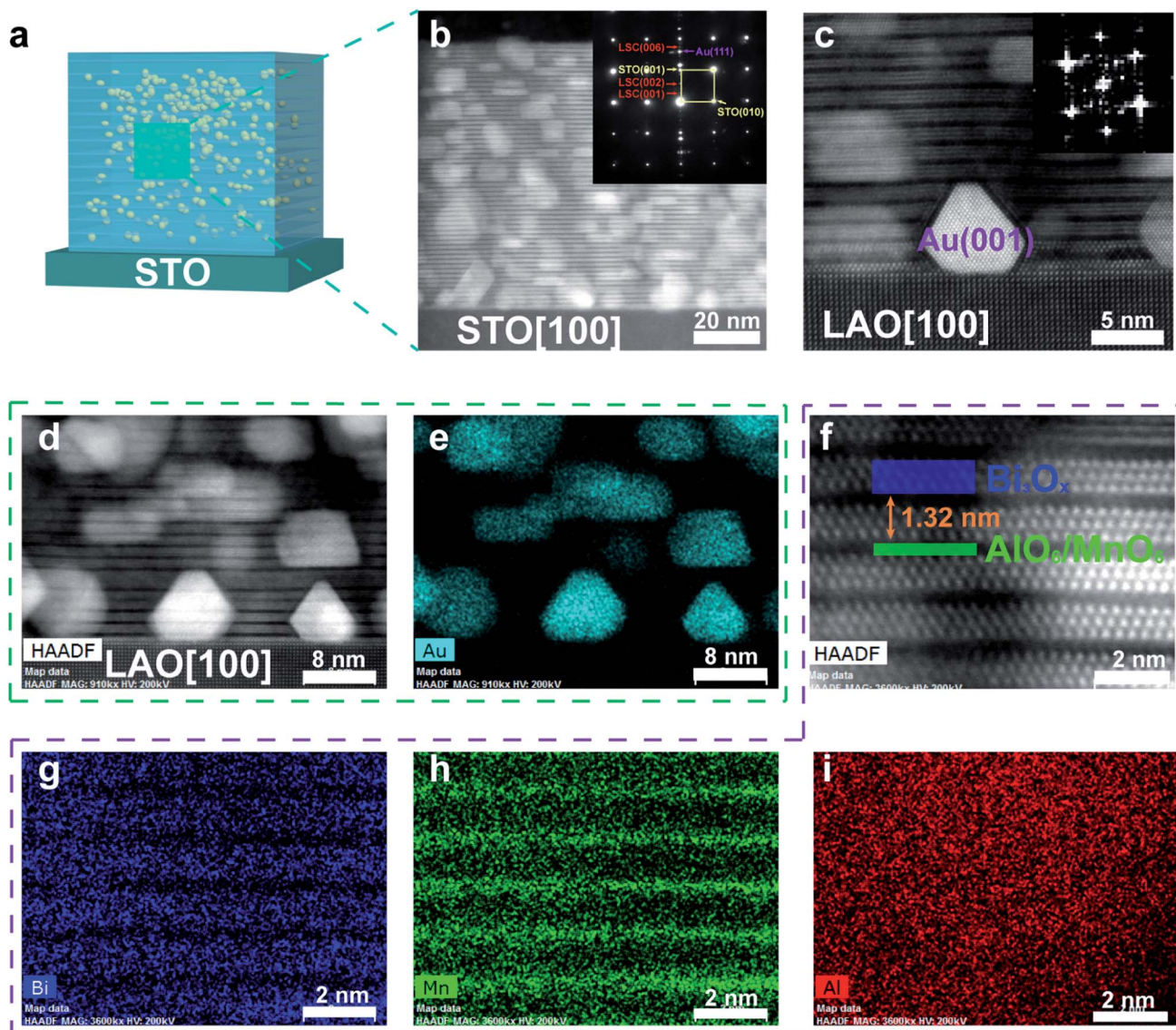


Fig. 2 Microstructure characterization of BAMO-Au thin films. (a) A schematic drawing of the BAMO-Au thin film. (b) High-resolution STEM image of the BAMO-Au thin film taken along the STO[100] zone axis. The inset shows the SAED pattern of the thin film and the substrate. (c) High-resolution STEM image of the BAMO-Au thin film taken along the LAO[100] zone axis. Au NPs are (001)-oriented at the interface between the substrate and the film. (d) High-resolution STEM HAADF image and (e) EDS map of the Au NPs embedded in the matrix. (f) High-resolution STEM HAADF image and (g, h and i) EDS maps together show the layered structure of the BAMO matrix.
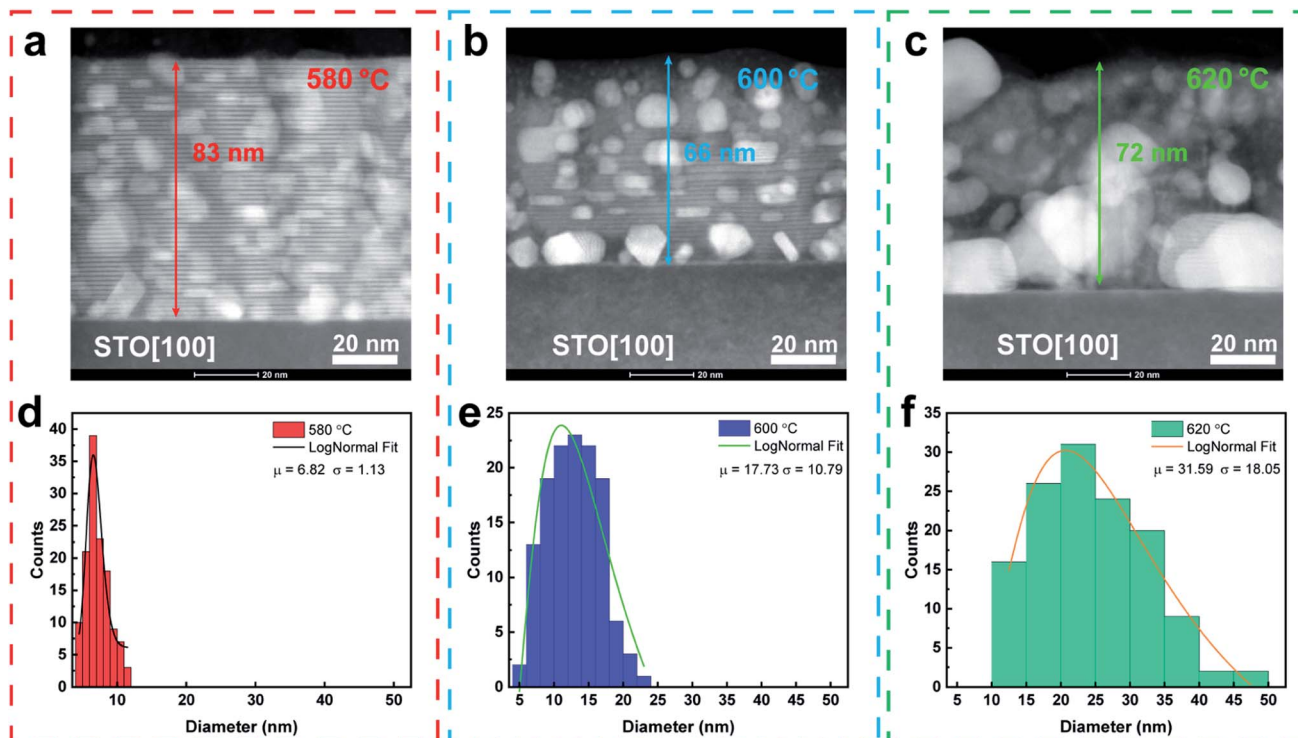
**Fig. 3** Size analysis of Au NPs in BAMO-Au thin films. (a)−(c) Cross-sectional STEM images of BAMO-Au thin films grown on the STO(001) substate at 580 °C, 600 °C, and 620 °C, respectively. (d)−(f) Histogram distribution analysis of the diameter of Au NPs along with the Lognormal fitting curve. The mean diameter of Au NPs is calculated for each temperature. The result clearly shows the size increase of Au NPs with deposition temperature.

meaning that (111)-oriented Au NPs are dominant. The more preferred (111) orientation of Au NPs is a result of the total surface free energy minimization according to Wulff's theorem, where the (111) crystal plane is the closely packed plane in the FCC structure and has the lowest surface energy. Thus, the Au (111) crystal plane is energetically favorable when forming NPs. The (001)-oriented Au NPs are found at the interface between the LAO substrate and the film as shown in Fig. 2c, where the (001) orientation is confirmed by the inset FFT image. The (001)-oriented growth at the interface can possibly be attributed to the low interfacial energy between LAO and Au NPs. The BAMO matrix is stabilized by alternating Bismuth oxide slabs and manganese/aluminum oxide octahedral layers along the film growth direction as shown in Fig. 2f.[15] The dark contrast phase is the Mn/Al-rich phase whereas the bright contrast phase is attributed to the Bi-rich layer. This is due to the Z-contrast mechanism for HAADF-STEM imaging, where Bi has a higher atomic number ($Z_{Bi}$ = 83) than Mn and Al ($Z_{Mn}$ = 25, $Z_{Al}$ = 13). The out-of-plane $d$-spacing is estimated to be 1.32 nm, which agrees with the XRD results. Fig. 2g–i display the EDS mapping analysis which clearly demonstrates the layered distribution of Bi, Mn and Al elements. It's noted that the uniform distribution of Al in the layered BAMO films might not reflect the true nature of the structure and such features could be attributed to several factors including the limited resolution of the TALOS TEM/STEM tool in resolving the light elements as well as the potential ion-milling induced damage during TEM sample preparation.

Fig. 3a–c present three cross-sectional HAADF-STEM images of BAMO-Au thin films grown on the STO(001) substrate at different deposition temperatures showing tunable growth morphologies. The films were grown at three deposition temperatures, *i.e.*, 580 °C, 600 °C, and 620 °C, respectively. The films thickness was kept in a similar range as the temperature varies as shown in Fig. 3, which is about 80 nm thick after 3000-pulse deposition. The slightly lower thickness in the samples deposited at 600 °C and 620 °C in the STEM images is due to the ion beam damage during the ion milling process resulted in a thinner TEM foil for the samples. Therefore, the growth rate of the films is estimated to be about 0.27 Å/pulse. The STEM images clearly show the distinct morphology variation as deposition temperature increases. This is manifested in two ways. First, the average diameter of the Au NPs increases from 6.82 (±1.13) nm to 17.73 (±10.79) nm to 31.59 (±18.05) nm as the temperature increases from 580 °C to 600 °C to 620 °C as shown in Fig. 3d–f, respectively. Second, the layered structure of the BAMO matrix is distorted as temperature increases from 580 °C to 620 °C. At 580 °C, the Au NPs are randomly distributed in the BAMO LSC matrix, and the layered structure is well preserved. As the temperature increases to 600 °C, the layered structure is moderately distorted and the diameter of Au NPs increases as well. At 620 °C, the size of the Au NPs is significantly enlarged and the LSC structure of the matrix is no longer maintained. The dependence of the Au NP size on the deposition temperature can be attributed to the mobility of adatoms. At higher growth temperatures, the diffusion of adatoms is

facilitated, which leads to higher mobility and larger Au nanoparticles. In addition, at higher growth temperatures, small Au NPs are prone to coalescing into larger NPs as reported previously.[46] The morphology variation of the LSC matrix could be attributed to two factors. On the one hand, higher deposition temperature deviates from the inherent optimum deposition temperature of the LSC structure, causing the degradation of the matrix. On the other hand, the larger Au NPs further distorted the LSC growth at high temperature. The shape of the Au NPs is not uniform with mostly being sphere-like and a small portion being disc-like as confirmed by Fig. 3a–c coupled with plan-view STEM images (Fig. S3†).

Au is a well-studied plasmonic metal, and its NPs have been proposed to have a variety of applications in many fields, such as non-toxic carriers for drug delivery, optical trapping and manipulation.[31,33] Therefore, it's conceivable that the Au NPs in the BAMO-Au thin films coupled with the anisotropic LSC structure would exhibit intriguing optical properties. The transmittance of BAMO-Au thin films on the STO substrate was measured and the data are plotted in Fig. 4a. In contrast to the smoothly increasing transmittance curve for the pure BAMO thin film, the BAMO-Au thin films show strong plasmonic absorption within the wavelength range from 700 to 800 nm as marked by arrows in Fig. 4a. It is noted that there is a sharp drop

at about 380 nm (3.25 eV), which is attributed to the indirect band gap absorption of the STO substrate.[47] A similar plasmonic absorption is observed for BAMO-Au thin films grown on the LAO substrate as shown in Fig. S4a.† The bandgaps for BAMO-Au thin films are determined to be 2.7 eV, 2.8 eV and 2.5 eV for growth temperatures of 580 °C, 600 °C, and 620 °C using the Tauc method as shown in Fig. S4b.† The bandgap variation may be due to the size-dependent work function of Au NPs which causes band structure reconstruction at the Au NP and BAMO interface and leads to a change of electron density in the BAMO matrix and effectively tunes the bandgap of the nanocomposites at different temperatures.[43,48,49] The non-monotonous change of the bandgap for films grown at 620 °C further reflects the fact that their microstructure is seriously distorted. Therefore, their band structure is not just affected by the Au size but also the microstructure, which explains why the bandgap changes non-monotonously with the Au NP size. The strong absorption can be attributed to the LSPR of Au NPs. Based on the data, the possible influence of the Au interband transition on the overall BAMP bandgap measurement could exist but might be minimal considering the well separated BAMO band edge and the Au resonance peak position. In addition, the pure BAMO film without Au has a similar bandgap absorption wavelength to that of the BAMO-Au film, further
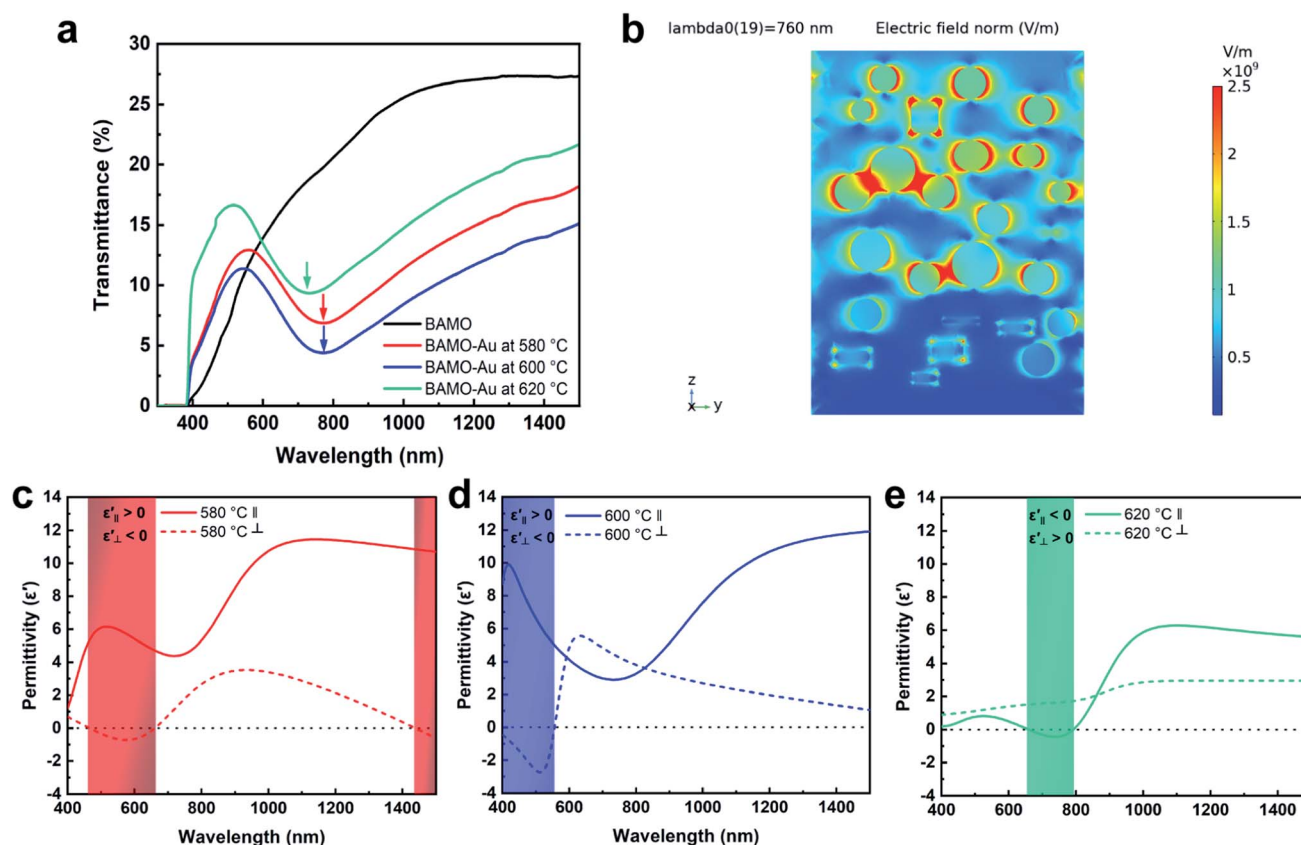


Fig. 4 Optical characterization of the BAMO–Au system. (a) Optical transmission spectra of BAMO–Au thin films as a function of wavelength. (b) Simulation of LSPR and local field enhancement effects using COMSOL Multiphysics® software. (c)–(e) Fitted permittivity for thin films deposited at different temperatures. Films grown at 580 °C and 600 °C display a type I hyperbolic dispersion, and the film grown at 620 °C shows a type II hyperbolic dispersion.

confirming the minor impacts. Using COMSOL Multiphysics® simulation, the LSPR of the BAMO-Au thin film grown at 580 °C was simulated and is plotted in Fig. 4b. The plasmonic peak wavelength is determined to be 760 nm as confirmed by the transmittance results. The plasmonic effect is remarkably attenuated at shorter and longer wavelengths as shown in Fig. S5.† The strong local-field enhancement effect (hot spots) is shown surrounding the Au NPs, and is particularly significant at the particle–particle edges due to the highly localized excitation probability, which is consistent with the previous report.[32] The optical dielectric permittivity of the BAMO-Au thin films was evaluated using a spectroscopic ellipsometer (JA Woollam RC2). Fig. 4c–e show the fitted permittivity of the BAMO-Au thin films deposited at three temperatures. The dielectric permittivity clearly displays anisotropy along IP and OP directions. Overall, the IP permittivity is larger than the OP permittivity in the majority wavelength range of the spectrum. This may be explained by the layered structure of the matrix. Since the matrix is an insulating dielectric material, the thin films have a typical positive value along the IP direction. In the out-of-plane direction, the permittivity of the thin films is depressed due to the presence of Au NPs, which have a negative permittivity within the visible light and near-infrared spectrum. More interestingly, all three films display hyperbolic behavior within the visible light region. While thin films grown at 580 °C and 600 °C have a Type I hyperbolic response ($\varepsilon_{xx}$, $\varepsilon_{yy} > 0$; $\varepsilon_{zz} < 0$), thin films grown at 620 °C have a Type II hyperbolic response ($\varepsilon_{xx}$, $\varepsilon_{yy} < 0$; $\varepsilon_{zz} > 0$).[50] The difference could be owing to the disparate microstructures of the thin films. As discussed earlier, the thin films grown at 580 °C and 600 °C both exhibit a layered structure. The thin film grown at 620 °C, however, doesn't preserve the layered structure. Therefore, the structural change in the matrix and enlarged Au NPs in the 620 °C sample could be the main reasons for the Type II hyperbolic properties.

It was previously reported that BAMO thin films show room-temperature multiferroic properties.[13,15] Interestingly, these properties are also preserved for the BAMO-Au thin films grown at 580 °C with a well-ordered LSC structure as shown in Fig. 5. The ferromagnetic properties of BAMO-Au thin films are shown in Fig. 5a and b for OP and IP, respectively. All the thin films exhibit obvious ferromagnetic responses in both IP and OP directions while the ferroelectric response was only observed for the film grown at 580 °C. The ferromagnetic properties of Aurivillius phase materials with the composition of $BiM_TMnO$ ($M_T$ is the transition metal) originate from the double-exchange coupling interaction between $Mn^{3+}$ and $Mn^{4+}$ cations, while the Bi $6s^2$ "lone pair" electrons of the pseudo-perovskite structure give rise to ferroelectric properties.[3,11,15,19,51] At higher deposition temperatures such as 600 °C and 620 °C, the presence of $Mn^{3+}$ and $Mn^{4+}$ continues to help preserve the ferromagnetic properties. However, since the pseudo-perovskite structure of the matrix was degraded due to the enlarged Au NPs, the ferroelectric properties were no longer maintained beyond 580 °C. Fig. 5a and b show the ferromagnetic response of the BAMO-Au thin films along IP and OP directions. There is a preferred out-of-plane magnetic anisotropy, and the

temperature has obvious effects on the ferromagnetic response, which could be explained by morphology variation of the thin films. From the HR-STEM images (Fig. 2), the BAMO-Au films show obvious structure anisotropy consisting of an alternating stacking of $Bi_3O_x$ and $AlO_6/MnO_6$ layers. The ferromagnetic properties are attributed to the double exchange coupling between the $Mn^{3+}$ and $Mn^{4+}$. The anisotropic saturation magnetization could be the result of such distinct structures along IP and OP directions. Such anisotropic magnetic properties have been reported in several layered oxide systems as well as other thin film systems.[12,13,15,24,52–55] Fig. S8† shows the saturation magnetization and coercive field of the thin films as a function of deposition temperature. The saturation magnetization ($M_s$) is determined to be ~4.0 emu cm$^{-3}$, ~1.68 emu cm$^{-3}$, and ~2.74 emu cm$^{-3}$ for 580 °C, 600 °C, and 620 °C, respectively, at 300 K along the OP direction. In addition, the $M_s$ along the IP direction is measured to be ~2.6 emu cm$^{-3}$, ~0.98 emu cm$^{-3}$, and ~0.72 emu cm$^{-3}$ for 580 °C, 600 °C, and 620 °C, respectively. Clearly, the well-preserved LSC structure at 580 °C gives the highest saturation magnetization value, and distorted LSC structures have weaker magnetic properties. Fig. 5c shows a clear phase and amplitude switching behavior of the BAMO-Au thin film grown at 580 °C, demonstrating the switchable ferroelectric nature of the thin film. Fig. 5d displays a phase mapping image of the thin film characterized by PFM, and the distinct contrast demonstrates a vertical domain switching. The ferroelectricity of BAMO-Au is caused by the non-centrosymmetric structure. A pair of $Bi^{3+}$ valence electrons in the 6s orbital is not engaged in the sp orbital hybridization, which forms a local dipole moment and creates a ferroelectric polarization as reported previously.[4] At higher temperatures, the layered oxide structure of the matrix is destroyed due to the larger Au NPs, and as a result the ferroelectricity disappears. The $d_{33}$ ferroelectric coefficient curve and polarization hysteresis loop are shown in Fig. S9.† Note that the shape of the hysteresis loop is not typical, which is possibly due to the leaky channels of Au NPs. The largest $d_{33}$ value is determined to be 60 pm V$^{-1}$, and the saturation polarization and coercive field are 6 μC cm$^{-2}$ and 30 kV cm$^{-1}$, respectively. To investigate the interplay between the multiferroics and plasmonic metal phase, we explored the coupling effect between these two phases. Fig. 5e shows the polar MOKE (Magneto-optical Kerr effect) hysteresis loop for films grown at 580 °C. The measurement set-up is illustrated in Fig. 5f. Although the actual measuring wavelength is around 633 nm for MOKE measurements, which is not the plasmonic resonance wavelength of the films, a notable sign of magneto-optical coupling is revealed from this measurement. However, due to the limitation of the laser wavelength for the MOKE system, the measurement was conducted at 633 nm, which was in the range of the broad plasmonic resonance peak for the samples, not at the peak wavelength. The magneto-optical coupling properties could be further enhanced if the MOKE measurements were conducted at the plasmonic resonance peak of 760 nm. The MOKE measurement results display the potential of the BAMO-Au system as a candidate for optical-switching
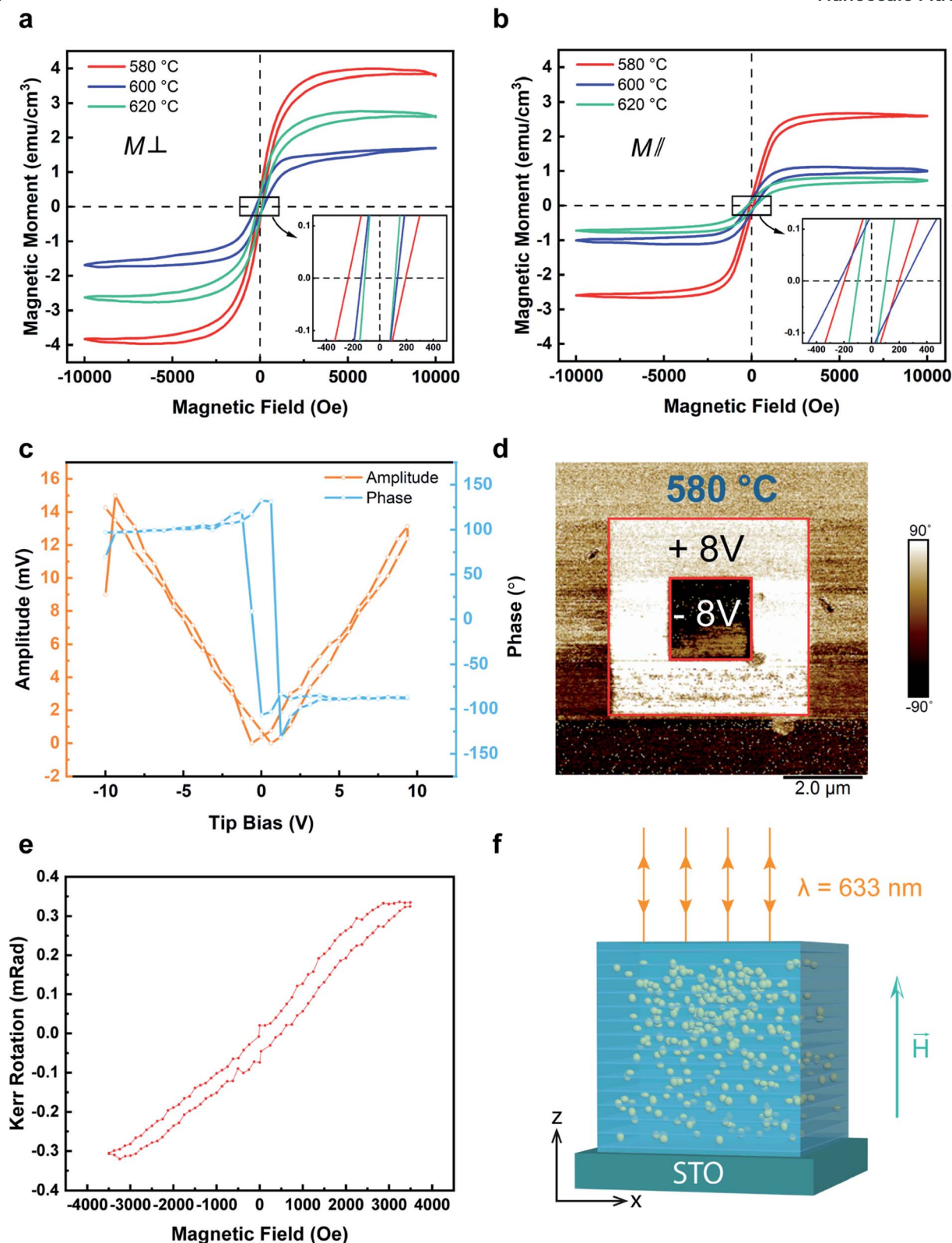
**Fig. 5** Multiferroic properties of the BAMO-Au system. (a) and (b) Ferromagnetic response of BAMO-Au thin films along out-of-plane and in-plane directions, respectively. The insets are the enlarged center area of the ferromagnetic hysteresis hoop showing the coercive field. (c) Amplitude and phase switching behavior as a function of tip bias for the BAMO-Au thin film grown at 580 °C. (d) Vertical PFM phase map for the BAMO-Au thin film grown at 580 °C, obtained by poling with +8 V (bright contrast) over $5 \times 5$ μm$^2$ and −8 V (dark contrast) over $2 \times 2$ μm$^2$. The outer area is not poled with voltage, and therefore has a random inherent phase. (e) Polar MOKE measurements for BAMO-Au films deposited at 580 °C. The magnetic field is applied along the out-of-plane direction. The hysteresis loop shows the magneto-optical coupling effect. (f) The experimental configuration for Polar MOKE measurements. The magnetic field is applied along the out of plane direction. The wavelength of the applied laser is about 630 nm.

spintronic devices. Based on the above MOKE results, we've demonstrated magnetic-switching *via* incoming laser light in the hybrid films. Conversely, considering the coexistence of the multiferroic phase and the plasmonic metal phase (*i.e.*, Au), we expect that the magnetization could be switched by applying an ultrafast laser (femtosecond) at the plasmonic resonance wavelength, aiming for all-optical-switching spintronic devices similar to some of the previous demonstrations.[20-22] Future work is needed for demonstrating such optical-switching potential in these hybrid systems.

Overall, our demonstration suggests the effectiveness of deposition temperature in tuning the morphology and properties of the BAMO-Au system. In comparison to the previously reported composition tuning method, temperature tuning provides a more effective and facile approach for tailoring the microstructure and physical properties. To the best of our knowledge, this is the first study to incorporate Au nanoparticles into the layered oxide systems for combined and coupled functionalities including ferromagnetic, ferroelectric and optical properties all in one system. Future directions could include incorporating other plasmonic metals (*e.g.*, Ag, Co) into the systems for effective coupling in different and specific wavelength ranges, and further tuning the distribution and morphologies of metal NPs for precise control of the plasmonic resonance wavelength. Another possible direction is to explore VAN nanostructures with layered oxide as the matrix since VAN can provide an extra degree of freedom through the vertical strain at the matrix/pillar heterointerface, enabling more effective tuning of the morphology and physical properties. One can also make multilayer nanocomposites with layered oxide and other functional components, providing a more straightforward approach for coupling multifunctionalities than other nanostructures.

## Conclusions

In summary, a novel oxide–metal hybrid material system consisting of the LSC BAMO matrix with Au NPs has formed a PIM system and presented rich multifunctionalities including LSPR, room-temperature multiferroic properties, and a hyperbolic response within the visible light spectrum. In addition, BAMO-Au shows interesting magneto-optic coupling between the multiferroic matrix and Au NPs. Morphology tuning of BAMO-Au thin films by controlling the deposition temperature has been demonstrated as an effective approach to tailor the microstructure and physical properties. The microstructure evolves from a perfect PIM layered structure to the formation of stacks of Au NPs with increasing deposition temperature, and the Au NPs get enlarged with deposition temperature. Such morphology variation effectively tunes the physical properties including ferromagnetic and ferroelectric responses, and anisotropic dielectric permittivity, with a hyperbolic response in certain wavelength ranges. This work provides new tuning approaches in Bi-based multiferroic layered oxides and effective coupling of plasmonic metals in multiferroic systems, which could lead to future optical-switching spintronics and memory devices.

## Author contributions

J. S. and H. W.* conceived the idea, designed all the experiments, and formulated the mechanistic understanding. J. S. implemented the XRD characterization work. J. S., Z. H. and D. Z. conducted the transmittance measurements and fitted the dielectric permittivity. J. S., Z. H., D. Z., Z. S., J. D. and P. L. together contributed to the STEM and EDS characterization work. J. S. and M. K. conducted the magnetic measurements. J. S. conducted the PFM characterization and electrical characterization work and accomplished the COMSOL simulation. H. H. W. and X. X. conducted the MOKE measurements. The manuscript was written through contributions of all authors. All authors have given approval to the final version of the manuscript.

## Conflicts of interest

The authors declare no competing financial interest.

## Abbreviations

| | |
|---|---|
| LSC | Layered supercell; |
| PIM | Particle-in-matrix; |
| BAMO | $Bi_{1.25}AlMnO_{3.25}$; |
| NPs | Nanoparticles; |
| LSPR | Localized surface plasmon resonance |

## Acknowledgements

## References

1 M. M. Vopson, *Crit. Rev. Solid State*, 2015, **40**, 223–250.

2 T. Kimura, S. Kawamoto, I. Yamada, M. Azuma, M. Takano and Y. Tokura, *Phys. Rev. B: Condens. Matter Mater. Phys.*, 2003, **67**, 180401.

3 W. Eerenstein, N. D. Mathur and J. F. Scott, *Nature*, 2006, **442**, 759–765.

4 M. Fiebig, T. Lottermoser, D. Meier and M. Trassin, *Nat. Rev. Mater.*, 2016, **1**, 16046.

5 E. Ascher, H. Rieder, H. Schmid and H. Stössel, *J. Appl. Phys.*, 1966, **37**, 1404–1405.

6 A. K. Pradhan, K. Zhang, D. Hunter, J. B. Dadson, G. B. Loiutts, P. Bhattacharya, R. Katiyar, J. Zhang, D. J. Sellmyer, U. N. Roy, Y. Cui and A. Burger, *J. Appl. Phys.*, 2005, **97**, 093903.

7 Y. H. Chu, L. W. Martin, Q. Zhan, P. L. Yang, M. P. Cruz, K. Lee, M. Barry, S. Y. Yang and R. Ramesh, *Ferroelectrics*, 2007, **354**, 167–177.

8 N. A. Spaldin and R. Ramesh, *Nat. Mater.*, 2019, **18**, 203–212.

9 S.-W. Cheong and M. Mostovoy, *Nat. Mater.*, 2007, **6**, 13–20.

10 W. Prellier, M. P. Singh and P. Murugavel, *J. Phys.: Condens. Matter*, 2005, **17**, R803–R832.

11 A. Chen, H. Zhou, Z. Bi, Y. Zhu, Z. Luo, A. Bayraktaroglu, J. Phillips, E. Choi, J. L. MacManus-Driscoll, S. J. Pennycook, J. Narayan, Q. Jia, X. Zhang and H. Wang, *Adv. Mater.*, 2013, **25**, 1028–1032.

12 X. Gao, L. Li, D. Zhang, X. Wang, J. Jian, Z. He and H. Wang, *Nanoscale*, 2020, **12**, 5914–5921.

13 L. Li, P. Boullay, P. Lu, X. Wang, J. Jian, J. Huang, X. Gao, S. Misra, W. Zhang, O. Perez, G. Steciuk, A. Chen, X. Zhang and H. Wang, *Nano Lett.*, 2017, **17**, 6575–6582.

14 Z. He, X. Gao, D. Zhang, P. Lu, X. Wang, M. Kalaswad, B. X. Rutherford and H. Wang, *Nanoscale*, 2021, **13**, 16672–16679.

15 S. Misra, L. Li, X. Gao, J. Jian, Z. Qi, D. Zemlyanov and H. Wang, *Nanoscale Adv.*, 2019, **2**, 315–322.

16 L. Pálová, P. Chandra and K. M. Rabe, *Phys. Rev. B: Condens. Matter Mater. Phys.*, 2010, **82**, 075432.

17 E. Choi, T. Fix, A. Kursumovic, C. J. Kinane, D. Arena, S. Sahonta, Z. Bi, J. Xiong, L. Yan, J. Lee, H. Wang, S. Langridge, Y. Kim, A. Y. Borisevich, I. MacLaren, Q. M. Ramasse, M. G. Blamire, Q. Jia and J. L. MacManus-Driscoll, *Adv. Funct. Mater.*, 2014, **24**, 7478–7487.

18 L. Li, W. Zhang, F. Khatkhatay, J. Jian, M. Fan, Q. Su, Y. Zhu, A. Chen, P. Lu, X. Zhang and H. Wang, *ACS Appl. Mater. Interfaces*, 2015, **7**, 11631–11636.

19 W. Zhang, M. Li, A. Chen, L. Li, Y. Zhu, Z. Xia, P. Lu, P. Boullay, L. Wu, Y. Zhu, J. L. MacManus-Driscoll, Q. Jia, H. Zhou, J. Narayan, X. Zhang and H. Wang, *ACS Appl. Mater. Interfaces*, 2016, **8**, 16845–16851.

20 A. V. Kimel and M. Li, *Nat. Rev. Mater.*, 2019, **4**, 189–200.

21 M. L. M. Lalieu, R. Lavrijsen and B. Koopmans, *Nat. Commun.*, 2019, **10**, 110.

22 L. Avilés-Félix, A. Olivier, G. Li, C. S. Davies, L. Álvaro-Gómez, M. Rubio-Roy, S. Auffret, A. Kirilyuk, A. V. Kimel, Th. Rasing, L. D. Buda-Prejbeanu, R. C. Sousa, B. Dieny and I. L. Prejbeanu, *Sci. Rep.*, 2020, **10**, 5211.

23 S. Misra, L. Li, D. Zhang, J. Jian, Z. Qi, M. Fan, H. Chen, X. Zhang and H. Wang, *Adv. Mater.*, 2019, **31**, 1806529.

24 X. Gao, L. Li, J. Jian, H. Wang, M. Fan, J. Huang, X. Wang and H. Wang, *ACS Appl. Nano Mater.*, 2018, **1**, 2509–2514.

25 H. Zheng, J. Wang, S. E. Lofland, Z. Ma, L. Mohaddes-Ardabili, T. Zhao, L. Salamanca-Riba, S. R. Shinde, S. B. Ogale, F. Bai, D. Viehland, Y. Jia, D. G. Schlom, M. Wuttig, A. Roytburd and R. Ramesh, *Science*, 2004, **303**, 661–663.

26 H. Wang, L. Li, J. Huang, X. Gao, X. Sun and H. Wang, *Mater. Res. Lett.*, 2019, **7**, 418–425.

27 K. Au, X. S. Gao, J. Wang, Z. Y. Bao, J. M. Liu and J. Y. Dai, *J. Appl. Phys.*, 2013, **114**, 027019.

28 I. Fasaki, M. Kandyla, M. G. Tsoutsouva and M. Kompitsas, *Sens. Actuators, B*, 2013, **176**, 103–109.

29 A. Cavallaro, M. Burriel, J. Roqueta, A. Apostolidis, A. Bernardi, A. Tarancón, R. Srinivasan, S. N. Cook, H. L. Fraser, J. A. Kilner, D. W. McComb and J. Santiso, *Solid State Ionics*, 2010, **181**, 592–601.

30 H. Shinguu, M. M. H. Bhuiyan, T. Ikegami and K. Ebihara, *Thin Solid Films*, 2006, **506**, 111–114.

31 G. V. P. Kumar, S. Shruthi, B. Vibha, B. A. A. Reddy, T. K. Kundu and C. Narayana, *J. Phys. Chem. C*, 2007, **111**, 4388–4392.

32 K. Imura, H. Okamoto, M. K. Hossain and M. Kitajima, *Chem. Lett.*, 2006, **35**, 78–79.

33 M. Das, K. H. Shim, S. S. A. An and D. K. Yi, *Toxicol. Environ. Health Sci.*, 2011, **3**, 193–205.

34 V. Amendola, R. Pilot, M. Frasconi, O. M. Maragò and M. A. Iatì, *J. Phys.: Condens. Matter*, 2017, **29**, 203002.

35 Y. Jin, *Adv. Mater.*, 2012, **24**, 5153–5165.

36 E. A. Coronado, E. R. Encina and F. D. Stefani, *Nanoscale*, 2011, **3**, 4042–4059.

37 V. I. Belotelov, I. A. Akimov, M. Pohl, V. A. Kotov, S. Kasture, A. S. Vengurlekar, A. V. Gopal, D. R. Yakovlev, A. K. Zvezdin and M. Bayer, *Nat. Nanotechnol.*, 2011, **6**, 370–376.

38 G. Armelles, A. Cebollada, A. García-Martín and M. U. González, *Adv. Opt. Mater.*, 2013, **1**, 10–35.

39 B. Sepúlveda, J. B. González-Díaz, A. García-Martín, L. M. Lechuga and G. Armelles, *Phys. Rev. Lett.*, 2010, **104**, 147401.

40 J. B. González-Díaz, A. García-Martín, J. M. García-Martín, A. Cebollada, G. Armelles, B. Sepúlveda, Y. Alaverdyan and M. Käll, *Small*, 2008, **4**, 202–205.

41 S. Misra, L. Li, J. Jian, J. Huang, X. Wang, D. Zemlyanov, J.-W. Jang, F. H. Ribeiro and H. Wang, *ACS Appl. Mater. Interfaces*, 2018, **10**, 32895–32902.

42 G. Fu, X. Ning, M. Chen, S. Wang, P. Liu, J. Wang and X. Li, *J. Am. Ceram. Soc.*, 2019, **102**, 2761–2769.

43 Z. He, J. Jian, S. Misra, X. Gao, X. Wang, Z. Qi, B. Yang, D. Zhang, X. Zhang and H. Wang, *Nanoscale*, 2020, **12**, 17886–17894.

44 J. Lu, R. L. Paldi, Y. Pachaury, D. Zhang, H. Wang, M. Kalaswad, X. Sun, J. Liu, X. L. Phuah, X. Zhang, A. A. El-Azab and H. Wang, *Mater. Today Nano*, 2021, **15**, 100121.

45 L. Li, L. Sun, J. S. Gomez-Diaz, N. L. Hogan, P. Lu, F. Khatkhatay, W. Zhang, J. Jian, J. Huang, Q. Su, M. Fan, C. Jacob, J. Li, X. Zhang, Q. Jia, M. Sheldon, A. Alù, X. Li and H. Wang, *Nano Lett.*, 2016, **16**, 3936–3943.

46 T. Donnelly, S. Krishnamurthy, K. Carney, N. McEvoy and J. G. Lunney, *Appl. Surf. Sci.*, 2007, **254**, 1303–1306.

47 K. van Benthem, C. Elsässer and R. H. French, *J. Appl. Phys.*, 2001, **90**, 6156–6164.

48 N. T. Khoa, S. W. Kim, D.-H. Yoo, E. J. Kim and S. H. Hahn, *Appl. Catal., A*, 2014, **469**, 159–164.

49 H. Zheng, Y. Zhou and S. Gangopadhyay, *J. Appl. Phys.*, 2015, **117**, 024504.

50 A. Poddubny, I. Iorsh, P. Belov and Y. Kivshar, *Nat. Photonics*, 2013, 7, 948–957.

51 R. Seshadri and N. A. Hill, *Chem. Mater.*, 2001, **13**, 2892–2899.

52 M. Kalaswad, B. Zhang, X. Wang, H. Wang, X. Gao and H. Wang, *Nanoscale Adv.*, 2020, **2**, 4172–4178.

53 V. Fernandes, P. Schio, R. J. O. Mossanek, A. J. A. de Oliveira, W. A. Ortiz, D. Demaille, F. Vidal, Y. Zheng, P. Fichtner, L. Amaral, M. Abbate, J. Varalda, W. H. Schreiner and D. H. Mosca, *Electrochem. Solid-State Lett.*, 2011, **14**, P9.

54 E. D. L. Rienks, S. Wimmer, J. Sánchez-Barriga, O. Caha, P. S. Mandal, J. Růžička, A. Ney, H. Steiner, V. V. Volobuev, H. Groiss, M. Albu, G. Kothleitner, J. Michalička, S. A. Khan, J. Minár, H. Ebert, G. Bauer, F. Freyse, A. Varykhalov, O. Rader and G. Springholz, *Nature*, 2019, **576**, 423–428.

55 A. Kumar, D. K. Pandya and S. Chaudhary, *J. Appl. Phys.*, 2012, **111**, 073901.